Long Equatorial Waves in a High-Resolution OGCM Simulation of the Tropical Pacific Ocean during the 1985-94 TOGA Period

Jean-Philippe Boulanger, Pascale Delécluse, Christophe Maes, Claire Lévy

Long Equatorial Waves in a High-Resolution OGCM Simulation of the Tropical Pacific Ocean during the 1985–94 TOGA Period

J.-P. BOULANGER,* P. DELECLUSE, C. MAES, AND C. LÉVY

Laboratoire d'Océanographie Dynamique et de Climatologie, Unité Mixte de Recherche, CNRS/ORSTOM/UPMC, Paris, France

(Manuscript received 19 June 1995, in final form 7 December 1995)

ABSTRACT

A high-resolution oceanic general circulation model (OGCM) of the three tropical oceans is used to investigate long equatorial wave activity in the Pacific Ocean during the 1985–94 TOGA period. The ARPEGE atmospheric general circulation model simulated zonal wind stress forcing and the OPA OGCM simulated dynamic height are interpreted using techniques previously applied to data. Long equatorial waves of the first baroclinic mode (Kelvin and first-mode Rossby waves) are detected propagating in the model outputs during the entire period. A seasonal cycle and interannual anomalies are computed for each long equatorial wave. In the east Pacific basin, long equatorial wave coefficients are dominated by seasonal variations, while west of the date line they display strong interannual anomalies. Interannual long-wave anomalies are then compared to wave coefficients simulated by a simple wind-forced model. The results presented here indicate the major role played by wind forcing on interannual timescales in generating long equatorial waves. Discrepancies between the simple wave model and the OPA first-mode Rossby coefficients allow one to draw limitations of interpreting sea surface variability in terms of waves of the first baroclinic mode alone. Finally, the simple wave model cannot fully explain the Kelvin wave amplitude near the western boundary, nor the first-mode Rossby wave amplitude near the eastern boundary. However, coherency between the Kelvin and first-mode Rossby wave coefficients at both boundaries lead to the conclusion that reflection occurs in this model and contributes to the wave amplitudes as they propagate away from the boundaries.

1. Introduction

A major success of the 1985–94 TOGA (Tropical Ocean Global Atmosphere) program is the continuation and development of ocean observing systems such as Volunteer Observing System, Tropical Atmosphere Ocean (TAO) buoy array, Surface Velocity Program, etc. During the TOGA decade, Geosat and Topex/Poseidon satellite altimeters provided large-scale sea level measurements during two El Niño and one La Niña event. Both satellite data and in situ data from the TOGA–TAO buoy array contributed to a large-scale coverage and high-accuracy observations of the tropical Pacific Ocean (McPhaden 1993; Menkes et al. 1995) and allow us to investigate theoretical mechanisms hypothesized for El Niño–Southern Oscillation (ENSO) variability (Delcroix et al. 1994, hereafter D94; Kessler and McPhaden 1995; Boulanger and Menkes 1995, hereafter BM).

Various theories, such as the warm water buildup in the western Pacific Ocean (Wyrtki 1975), the delayed action oscillator mechanism (Schopf and Suarez 1988), or the SST mode in the fast wave limit (Neelin 1991) have been suggested to play a role in ENSO variability. In particular, the delayed action oscillator theory involves the linear ocean dynamics associated with the propagation and reflection of long equatorial waves (Battisti 1988). Mainly, the Kelvin and three gravest meridional mode Rossby waves are expected to play a dominant role in the equatorial ocean dynamics and ENSO variability (Battisti 1988). Kelvin waves were first observed in the meridional shape of their sea level signature (Ripa and Hayes 1981) and in the eastward propagating zonal velocity and sea level signals (Knox and Halpern 1982). First meridional mode Rossby waves were detected in in situ data by Lukas et al. (1984) and Lukas and Firing (1985). Using Geosat altimetric data, Miller et al. (1988) and later Delcroix et al. (1991) demonstrated clear propagation of these waves throughout most of the basin. Also using observations from the Geosat altimeter covering the 1986–87 El Niño and 1988–89 La Niña events, D94 described Kelvin and first-mode Rossby wave propagation over most of the tropical Pacific Ocean on ENSO-related variability and evaluated their contributions to sea level and geostrophic zonal current anomalies. But only with

*Current affiliation: Jet Propulsion Laboratory/California Institute of Technology, Pasadena, California

Corresponding address: Dr. J.-P. Boulanger, Jet Propulsion Laboratory, California Institute of Technology, MS 300-323, 4800 Oak Grove Drive, Pasadena, CA 91109.
E-mail: jpb@pacific.jpl.nasa.gov

the highly accurate Topex/Poseidon altimeter, have second- and third-mode Rossby waves been observed propagating at theoretical speeds (BM). Thus, while linear ocean dynamics and long equatorial waves were viewed as a useful conceptual approach for the understanding of low-frequency tropical oceanic variability, they are now quantitatively used to interpret sea level and zonal geostrophic current anomalies and, most of all, sea surface temperature variability (Picaut and Delcroix 1995).

All these studies relied on the hypothesis that the sea level variability can be explained by a sum of long equatorial waves of the first baroclinic mode alone. However, while examination of surface sea level and dynamic height variability confirmed the dominant role played by the first baroclinic mode, higher vertical modes have been shown to contribute to the surface and subsurface current variability (Lukas and Firing 1985; Giese and Harrison 1990). The purpose of our study is to estimate to what extent long equatorial wave coefficients presented as of the first baroclinic mode can indeed be explained by a single baroclinic mode linear ocean model. Unfortunately, this question cannot be assessed by comparing wind forcing and sea level variability over the whole tropical Pacific ocean on long timescales as we lack a large scale and high space–time density observing system. Thus, we decided to force a high-resolution oceanic general circulation model and a simple wave model by the same wind forcing and to compare their responses in terms of long equatorial waves. This approach allows us to identify the role played by the wind forcing, to identify potential longwave reflection, and to assess to what extent long equatorial waves of a single baroclinic mode can explain sea level variability.

The oceanic general circulation model (OGCM) we used was adapted to the tropical Pacific Ocean and tested in different experiments. The early runs were developed and extensively detailed by Dandin (1993). The model was included in a TOGA-NEG (Numerical Experiment Group) intercomparison (Stockdale et al. 1993), which quantified the typical biases of models forced by climatological conditions. The present version of the model differs slightly from that earlier version (mainly in spatial coverage and bottom and coastal topography). However, the physical parameters have similar values. The velocity fields from the run discussed here were compared to the seasonal mean drifter fields from the Surface Velocity Program and presented variances in both zonal and meridional velocity components similar to observations (P. Niiler 1995, personal communication).

The arrangement of this paper is as follows. In section 2, we describe the model in detail; in section 3, we describe the simulated fields, briefly present the method used for the calculation of long equatorial wave coefficients, estimate the variance of dynamic height and zonal wind stress explained by Kelvin and first-mode Rossby waves in the equatorial band, and present the simple wave model used to calculate the wind-forcing contribution to long equatorial wave coefficients; in section 4, we describe these coefficients, as well as their seasonal cycle; in section 5, we compare interannual anomalies simulated by the simple wave model to the projected long wave coefficients; and finally, in section 6, we summarize the individual propagation characteristics of long equatorial waves in the simulation of the TOGA period, and we discuss issues raised by this study.

2. Model

This study was performed with the OGCM developed at the Laboratoire D'Océanographie Dynamique et de Climatologie (LODYC) (OPA Version 7, Delecluse et al. 1993). It solves the primitive equations (i.e., Navier–Stokes equations plus some classic additional assumptions: Boussinesq and hydrostatic approximations, incompressibility), assuming the sea surface to be a rigid-lid boundary. The in situ density is computed following the formulation given in Millero and Poisson (1981). These equations are written in tensorial form so that they are suited to any three-dimensional orthogonal curvilinear mesh on the sphere. The use of vectorial operators ensures a second-order accuracy on the grid (Marti et al. 1992). The equations are discretized in finite differences on a staggered C grid (Arakawa 1972), and the finite difference equations can be found in Delecluse et al. (1993). The time stepping is achieved with a basic leapfrog differencing structure associated with an Asselin (1972) time filter, while a forward scheme is used for the turbulent horizontal diffusion terms and an implicit scheme for the turbulent vertical diffusion terms. The time step is set to 1 h. No-slip boundary conditions and no flux conditions for heat and salt are applied at the bottom and along the coastlines, while the surface fluxes of momentum, salinity, and heat are prescribed through the specification of the wind stress, the freshwater budget, the penetrative solar flux, and the net heat budget at the sea surface.

The subgrid physics are parameterized as follows. 1) Vertical mixing coefficients are computed from a level 1.5 turbulent closure model in which the turbulent kinetic energy (TKE) is computed through a prognostic equation, while the turbulent length scales are defined by a diagnostic formulation. This parameterization has been embedded in the LODYC OGCM by Blanke and Delecluse (1993) for tropical simulations. The delicate point of the closure assumption lies in the formulation of the turbulent length scale, which is defined as the length scale associated with conversion of the TKE into potential energy. 2) Lateral mixing is explicited by a second-order operator, and the value of the horizontal viscosity and diffusivity are positive constants equal to 10^3 m^2 s^{-1}. These magnitudes are taken following the sensitivity experiments presented by Maes et al. (1997). This study shows that a large value of these coefficients

(an order larger) can modify the large-scale response of the model and a low value (an order smaller) leads to an enhanced role of the vertical physics. The medium value is kept here in the equatorial region until 20°N and 20°S, and smoothly increases to the lateral boundaries.

The model domain covers the three tropical oceans between 50°N and 50°S. The mesh has a classic geographical configuration (latitude–longtitude), and the third axis is the local vertical. The zonal mesh is determined by analytical functions where the resolution is increased each time that a coastline crosses the equator. The zonal resolution is equal to 0.33°, increasing to 0.75° in the middle of the basins. The meridian resolution is also irregular with smallest value of 0.33° at the equator, increasing to 1.5° at the northern and southern boundaries. The vertical mesh is defined through 30 levels until a 5000-m threshold. The minimum resolution is set to 10 m in the 16 upper levels and increases after level 24 (deeper than 600 m). The bottom topography is derived from the 5′ × 5′ ETOPO5 dataset (Marine Geology and Geophysics Division, National Geophysical Data Center, Boulder, Colorado) averaged over each model grid box. The model includes a connection between the Indian and the Pacific Oceans.

The experimental forcing conditions (wind stress, heat fluxes, and fresh budget) are taken from the climate version of ARPEGE, whose main characteristics are presented by Déqué et al. (1994). The atmosphere model has been run during the TOGA period (1985–94) using the observed SST (Reynolds and Smith 1994) as a lower boundary condition. The forcing fields used in this study are extracted daily from the T42 spectral model. The surface heat flux is then parameterized as

$$Q = Q_{\text{Arpege}} + \frac{dQ}{dT}(\text{SST} - \text{SST}_{\text{ob}}),$$

where Q_{Arpege} is given by the atmosphere model, SST_{ob} is the observed sea surface temperature of Reynolds and Smith (1994), and SST is the first level temperature of the ocean model. The negative feedback term dQ/dT is set to -40 W m^{-2} K^{-1}, a typical value over the equatorial Pacific Ocean (Oberhuber 1988). The solar flux is allowed to penetrate below the top model layer; its attenuation with depth follows the formulation of Paulson and Simpson (1977) with a Jerlov (1968) optical water type I. The solar flux is absorbed into the first 10 m.

The model has closed boundaries along 50°N and 50°S. In order to avoid a slow drift due to the absence of a deep thermohaline circulation, temperature and salinity are restored toward the Levitus (1982) data (monthly mean for temperature, seasonal mean for salinity) below the mixed layer between the 20° and 50° latitudes. The mixed layer depth is estimated from the vertical mixing coefficient values calculated by TKE. The restoring coefficient value varies in function of depth and latitude [it increases poleward from (250 days)$^{-1}$ at 20°N and 20°S to (30 days)$^{-1}$ at the northern and southern boundaries]. The model starts in January, with Levitus salinity and temperature, and was spun up from rest (by repeating the 1984 year).

3. Zonal wind stress, dynamic height fields, and the simple wave model

We are interested in studying a simulation of the Pacific Ocean in a way similar to recent works on observed sea level, dynamic height, or geostrophic zonal current anomalies (e.g., D94; Kessler and McPhaden 1995; BM). Therefore, our study focuses on low-frequency surface dynamic height (relative to 1000 db) and zonal wind stress anomalies. Both fields have a 5-day time step and are filtered in time with a 55-day Hanning filter. The methods of Boulanger and Menkes (1995) were then used to project the zonal wind stress and dynamic height anomaly fields, respectively denoted $\tau_x(x, y, t)$ and $h(x, y, t)$, into the modes of long equatorial waves. Anomalies are computed relative to the 1985–94 mean. The reader is strongly suggested to refer to Boulanger and Menkes (1995) for a description of the decomposition methods. In the following, we briefly recall the basic assumptions of the method for projecting dynamic height. First, using simulated dynamic height anomalies, a time-lag correlation analysis was performed at the equator and at 4°N. A mean baroclinic phase speed of 2.5 m s^{-1} was estimated (the result will be detailed later). We used this value to estimate a Rossby radius (332 km) and then calculate long equatorial wave structures. In terms of surface dynamic height, it is assumed that

$$h(x, y, t) = \sum_{0}^{N} r_n(x, t)R_n^h(y),$$

where r_n are the coefficients to be calculated by the method and $R_n^h(y)$ are long-wave sea level structures (Fig. 1: $n = 0$ refers to Kelvin wave; n greater than 0 refers to the corresponding long Rossby wave). The sum is assumed to be finite [$N = 20$; see Boulanger and Menkes (1995) for a discussion on the value of N]. Only r_0 and r_1 are analyzed in the following. Zonal wind stress anomalies were similarly decomposed onto long equatorial wave structures following BM's method (see their appendix A4).

For each coefficient (Kelvin and first-mode Rossby), a time-lag correlation analysis (Delcroix et al. 1991) was used to calculate a mean phase speed and to estimate an error for this value. Results were for both wave coefficients 2.20 ± 0.5 m s^{-1} and -0.80 ± 0.5 m s^{-1}, respectively. They were thus consistent with our first estimate of 2.50 m s^{-1}. Then, a zonal wind stress field and a dynamic height field were reconstructed considering only Kelvin and first-mode Rossby signals. These reconstructed fields were compared to the original fields.

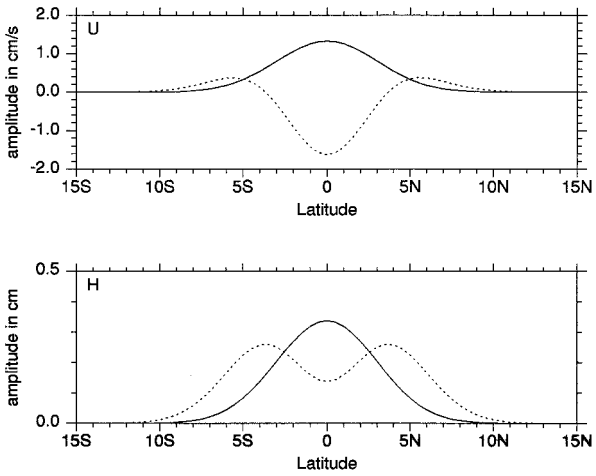

FIG. 1. Meridional structures of (a) zonal current and (b) sea level for Kelvin (solid line) and first Rossby (dotted line) modes calculated for a 2.5 m s^{-1} phase speed. Each wave contribution at a given latitude can be obtained by multiplying the meridional structure by the corresponding coefficient, yielding centimeters per second for zonal current, 0.001 Pa for zonal wind stress and centimeters for sea level (or dynamic height) anomaly.

a. Zonal wind stress

Figure 2a displays the standard deviation of the ARPEGE zonal wind stress. Regions of strong variability are located along the equator in the eastern Pacific from 150° to 110°W where the annual wind variability is known to be strong, in the western Pacific where the high-frequency wind variability is important, and mainly in the western Pacific poleward of 5°N and 5°S (not shown here) with a large amplitude near the date line associated with the interannual zonal wind stress variability. A zonal wind stress field was reconstructed using only the Kelvin and first-mode Rossby forcing coefficients. The correlation coefficients between the ARPEGE zonal wind stress field and the reconstructed field (Fig. 2b), as well as the variance of the ARPEGE zonal wind stress explained by the sum of the Kelvin and first-mode Rossby forcing terms (Fig. 2c), are very high along the equator, but both decrease rapidly poleward of 2°N–2°S. Thus, the zonal wind stress field reconstructed from the Kelvin and first-mode Rossby coefficients does not reproduce the entire pattern of strong variability located between 150° and 110°W, nor the off-equatorial maximum located in the western Pacific.

b. Dynamic height

The standard deviation of surface dynamic height anomalies is displayed in Fig. 3a. Major features are a strong variability west of the Galapagos Islands (oceanic response to the seasonal variability of zonal wind stress; see Fig. 2a), a high variability in the central Pacific and in the Northern Hemisphere (not entirely shown here), a similar amplitude in the off-equatorial western Pacific, but a weak variability in the extreme western Pacific region. A dynamic height field was reconstructed from the Kelvin and first-mode Rossby wave coefficients. The correlation coefficients between the simulated dynamic height anomalies and the reconstructed field (Fig. 3b), as well as the variance of dynamic height anomalies explained by the Kelvin and first-mode Rossby waves (Fig. 3c), are, respectively, higher than 0.9 and 90% throughout the Pacific Ocean in the 3°N–3°S band. Hence, all the equatorial variability observed in Fig. 3a (near the date line and in the east Pacific, both in conjunction with local maxima observed in the wind pattern) is fairly well explained.

4. Long equatorial wave seasonal cycle

It is worth recalling that zonal wind stress and dynamic height fields have a 5-day time step and are filtered with a 55-day Hanning filter. Thus, it is as well for long equatorial wave and forcing coefficients. Both wave and forcing coefficients are anomalies relative to the mean calculated over the 1985–94 period. A seasonal cycle is computed for each coefficient averaging years 1985 to 1994. Interannual anomalies are relative to this seasonal cycle. A first look at the Kelvin and first-mode Rossby wave coefficients (Figs. 4a and 4b) shows that the basin is mostly split into two regions. In the western part of the basin (west of the date line) interannual anomalies are more important, while in the eastern part the seasonal cycle is the strongest signal. To confirm this feature, we computed standard deviations of the wave coefficients, of their seasonal cycle, and of their interannual anomalies. Results are displayed in Figs. 5a and 5b. The Kelvin wave amplitude has a strong seasonal component east of 110°W. This feature is consistent with the large variability of zonal wind stress observed in Fig. 2a between 150° and 110°W. Indeed, equatorial zonal wind stress variations generate Kelvin waves that are propagating eastward of the anomalous wind patch, as well as first-mode Rossby waves propagating westward. A strong first-mode Rossby seasonal signal is indeed seen in Fig. 5b from 140°W to the date line. Interestingly, another important seasonal variability of the first-mode Rossby coefficient is detected near the eastern boundary (Fig. 5b). This pattern could be related to the reflection of Kelvin waves. This will be examined later.

In this section, we will focus on the seasonal cycle of the oceanic (Figs. 6b and 6d) and forcing (Figures 6a and 6c) Kelvin and first-mode Rossby coefficients. Interannual anomalies will be presented in the next section. Major events seen in Fig. 6 are detailed in the following. Westerly anomalies located near the date line in November–December forced a downwelling Kelvin wave (Fig. 6b) propagating into the eastern Pacific in January–February and a weak upwelling first-mode Rossby wave (Fig. 6d). As a consequence of the weakening of the trade winds in spring, a strong downwelling

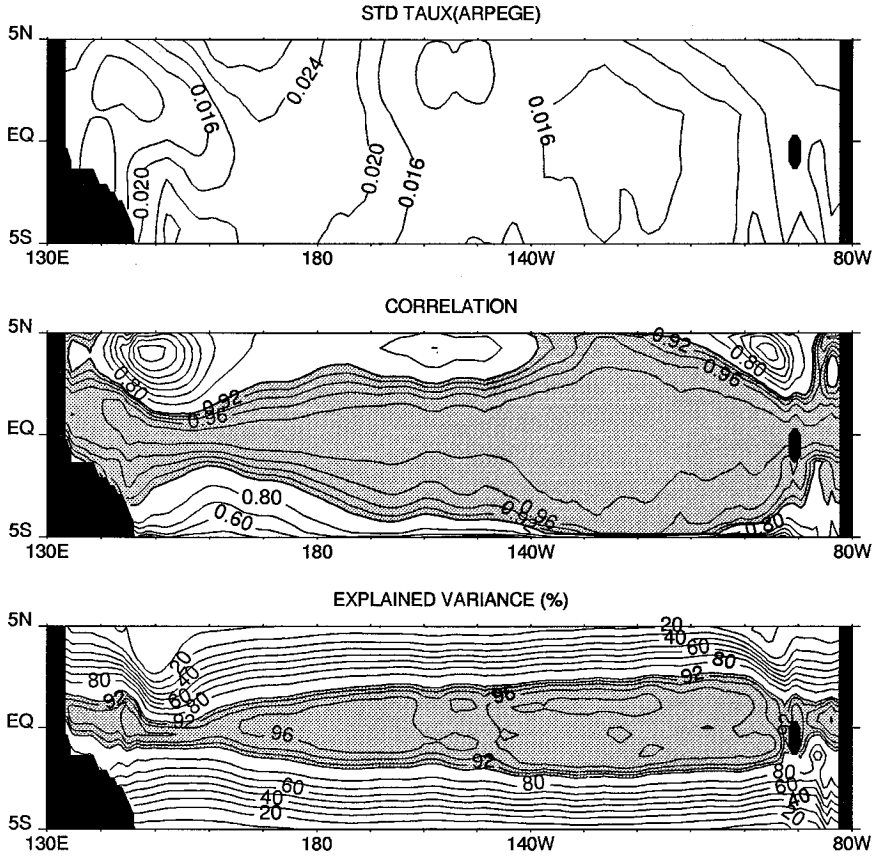

FIG. 2. (a) Standard deviation map of ARPEGE zonal wind stress over the 1985–94 period (units are pascals, contours are every 0.004 Pa); (b) map of correlation between ARPEGE zonal wind stress and zonal wind stress field reconstructed from only Kelvin and first-mode Rossby forcing coefficients (contour intervals are every 0.1 from 0 to 0.9, and every 0.04 from 0.90 to 0.98); (c) same as (b) but map of variance explained by the reconstructed field (contour intervals are every 10% from 10% to 90%, and every 4% from 90% to 98%).

Kelvin signal is present in the eastern Pacific and a strong upwelling first-mode Rossby wave is propagating westward. Both contribute to the seasonal warming of the eastern Pacific ocean as follows: they induce eastward current anomalies and contribute to the advection of warmer waters from the west, while the Kelvin wave deepens the thermocline in the east (therefore decreasing the cooling effect of upwelling on SST). It is worth noting that the annual upwelling first Rossby wave (Fig. 6d) is not coming from the eastern boundary but is wind forced from 110°W (Fig. 6a). Moreover, this wave is apparently propagating to the western boundary (Fig. 6d), but actually it is affected by the wind forcing located in the western Pacific in September. Indeed, the curve of the wave propagation is seen to flatten simultaneously with the presence of local forcing favorable to a first-mode Rossby downwelling signal. Then, during summer and fall, the trades reinforce inducing easterly anomalies that force upwelling Kelvin and downwelling first Rossby waves. The former will deepen the thermocline (i.e., switch dynamic height anomalies to positive values), and both waves will induce westward zonal currents. Therefore, they will contribute to the cooling of SST in the eastern Pacific. Although seasonal positive first-mode Rossby wind forcing in fall is located between 160° and 90°W (Fig. 6c), as the seasonal negative forcing is in spring, the downwelling first-mode Rossby wave is observed propagating from the eastern boundary in late spring (Fig. 6d). At this time, a strong downwelling Kelvin wave is reaching the boundary (Fig. 6b). Therefore, the downwelling first-mode Rossby wave seems to be generated by a reflection of the downwelling Kelvin wave and subsequently forced along its path by local winds. Reflection of Kelvin waves at the eastern boundary may thus play a role in the first-mode Rossby wave amplitude in spring (downwelling signal) and later in fall (upwelling signal) at least eastward of 110°W.

In the western part of the basin, the Kelvin seasonal cycle is rather weak (Fig. 6b). This might reflect that the wind variability in the western Pacific is dominated by high-frequency pulses (a few days to a few months). Therefore, the Kelvin wave variability is primarily high frequency and does not display strong recurrent features

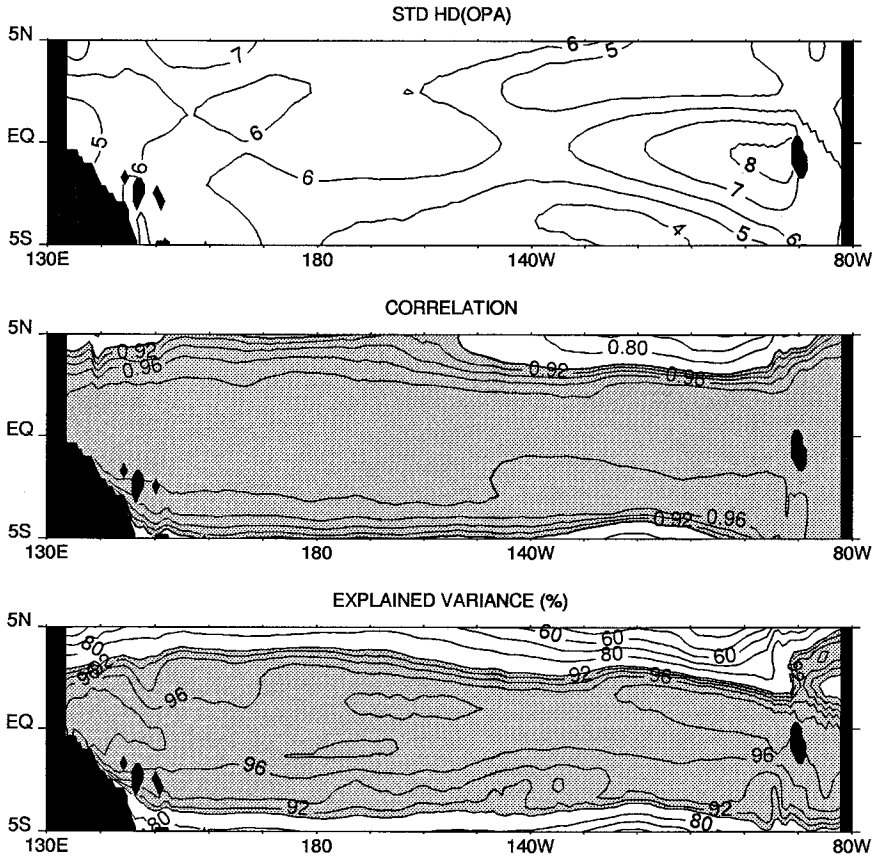

FIG. 3. Same as Fig. 2 but considering anomalous dynamic height field relative to 1000 db (anomalies are computed relative to the 1985–94 mean). Units of dynamic height standard deviation are centimeters. Contour intervals of the maps of correlation and of explained variance are as described in Fig. 2.

from one year to another, as the first-mode Rossby wave does in the eastern Pacific at the annual period. Therefore, by averaging several years to calculate a seasonal cycle, high-frequency signals will tend to cancel and the seasonal cycle would display a weak amplitude in the western Pacific.

5. Interannual variability and wind-forced contribution

To assess the role of the wind forcing in terms of baroclinic wave generation during the 1985–94 simulated period, we used a simple wind-forced baroclinic wave model. For each wave, forcing coefficients are integrated along wave characteristics from 130°E to 80°W for the Kelvin mode and from 80°W to 130°E for the first Rossby mode. For each wave, the model integrates the following equation:

$$(\partial_t + c_n\partial_x + r_n)a_n(x, t) = \frac{F_n(x, t)}{\rho_0 D},$$

where phase speeds of wave propagation (c_n) are assumed to be 2.5 and -0.83 m s^{-1}, r_n is a damping time taken to be (3 months)$^{-1}$ for Kelvin and first Rossby modes, F_n are the forcing coefficients, ρ_0 is the water density, D is an amplitude factor equivalent to the depth of a one-layer ocean model, and a_n are the coefficients to be calculated. No reflection at the boundaries is taken into account; thus, only wind forcing contribution is shown. The choice of the damping timescale was made by comparing the simple wave model and the OPA model. It is consistent with estimates made by Picaut et al. (1993) and Kessler and McPhaden (1995) comparing simple models and data. The amplitude factor D was estimated by comparing standard deviations of projected coefficients and integrated coefficients. Its value is taken to be 100 m. In the following, only comparisons between interannual anomalies of calculated wave coefficients from the simulated dynamic height anomalies (called OPA coefficients) and of integrated wave coefficients from the simple wind-forced model (called SIMO coefficients, SIMO for simple model) will be discussed. It is worth recalling that zonal wind stress and dynamic height fields have a 5-day time step and are filtered with a 55-day Hanning filter. Thus, it is the same for OPA and SIMO long equatorial wave coefficients.

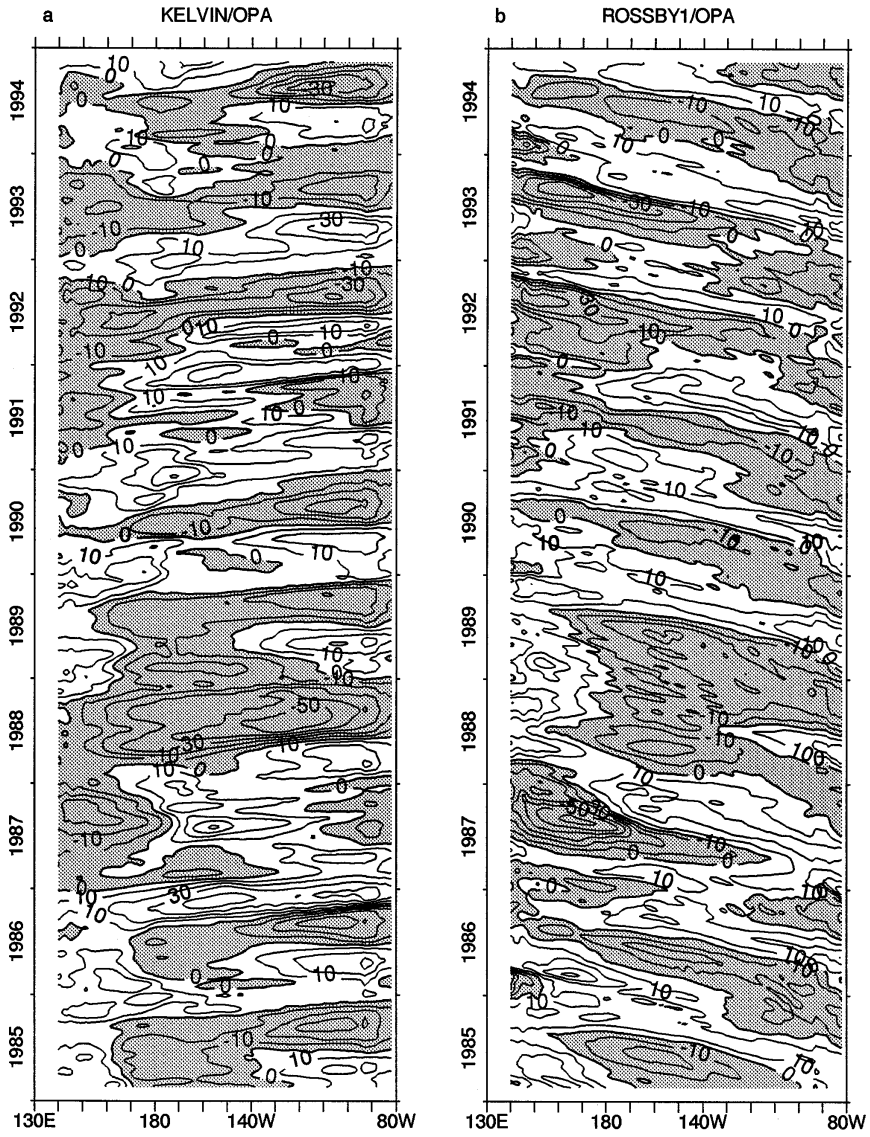

FIG. 4. Longitude time plots of (a) Kelvin and (b) first-mode Rossby wave coefficients. Coefficients are nondimensionalized. Contour intervals are every 10 units for the wave coefficients. An oceanic coefficient of 10 units would yield to a dynamic height anomaly of 3.2 cm of the Kelvin wave at the equator and of 2.8 cm of the first-mode Rossby wave at 4°N.

It is worth noting that interannual anomalies do not mean signals with periods longer than the annual period, but anomalies relative to a seasonal cycle. Therefore, interannual anomalies contain also high-frequency signals related to interannual variability (such as ENSO events). Before describing variability of the OPA and SIMO coefficients, we performed a comparison between OPA and SIMO Kelvin and first-mode Rossby coefficients. Results are displayed in Fig. 7. The correlation coefficient between OPA and SIMO Kelvin wave coefficients (Fig. 7a) is higher than 0.8 roughly from the date line to 110°W. Lower correlations are indeed observed near the western boundary where the SIMO coefficient (Fig. 7b) is much weaker than the OPA coefficient. In this region, reflection of long Rossby waves at the western boundary may indeed contribute to the Kelvin signal propagating westward. Poor correlation values are also found near and east of the Galapagos Islands. These islands appear to have a strong influence on the simulated oceanic signal in this region. Whether their influence is realistic or not will need to be examined. The correlation between OPA and SIMO first-mode Rossby wave coefficients (Fig. 7c) displays a strong maximum west of the date line (i.e., west of the region of interannual wind stress variability) and a local maximum near 110°W in the region of annual wind variability. However, the comparison is very poor near 160°W and near the eastern boundary. Two factors can

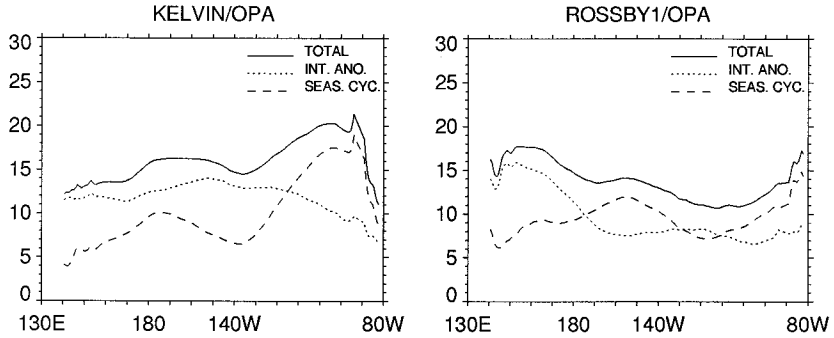

FIG. 5. (a) Standard deviation as a function of longitude from 130°E to 80°W of the Kelvin wave coefficient calculated from the simulated surface dynamic height relative to 1000 db: total signal (solid line), seasonal cycle (dotted line), and interannual anomalies (dashed line). Values are adimensionalized; (b) same as (a) but for the first-mode Rossby wave coefficient.

be responsible for the low correlation values near the eastern boundary: the presence of the Galapagos Islands (as mentioned above), and the existence of reflection of Kelvin waves into first-mode Rossby waves. The wind forcing (Fig. 7d, dashed line) has a weak amplitude east of 150°W. It seems that reflection of Kelvin waves may indeed contribute to the first-mode Rossby wave amplitude, at least to 150°W. While the wind-forcing contribution is too weak east of 150°W, it appears to be too strong westward (Fig. 7d). In particular, the rms differ-

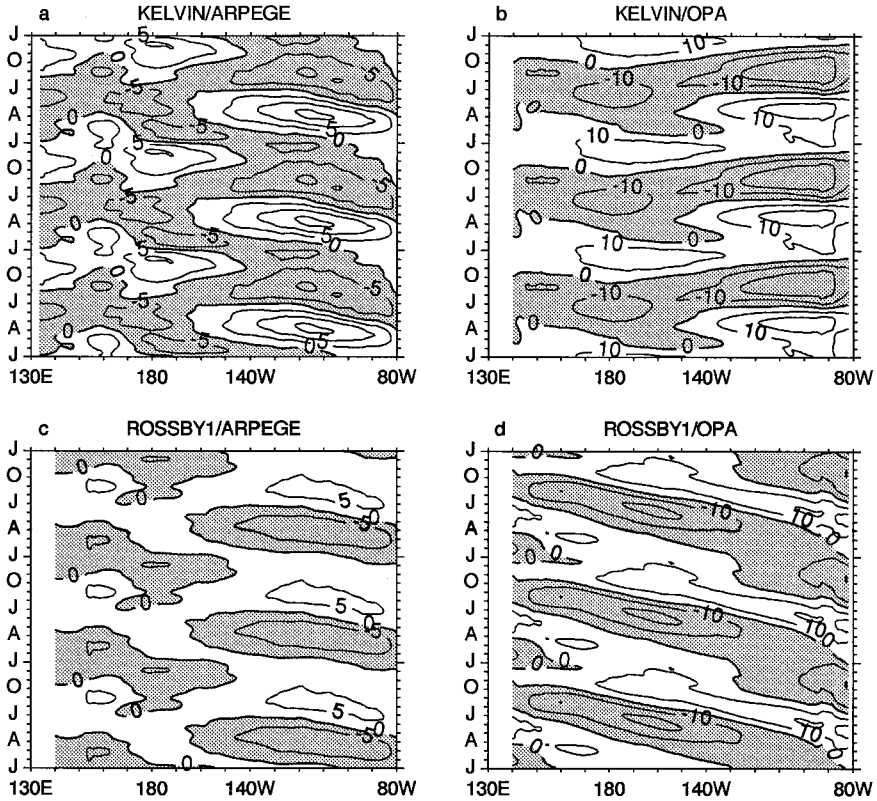

FIG. 6. Longitude time plots of the seasonal cycle of the (a) Kelvin forcing, (b) Kelvin wave, (c) first-mode Rossby forcing, and (d) first-mode Rossby wave coefficients. The seasonal cycle is repeated three times. Coefficients are nondimensionalized. Contour intervals are every 5 units for the forcing coefficients and 10 units for the wave coefficients. A forcing coefficient of 5 units would yield to an equatorial zonal wind stress amplitude of roughly 0.007 Pa of the Kelvin part and −0.009 Pa of the first-mode Rossby part. An oceanic coefficient of 10 units would yield to a dynamic height anomaly of 3.2 cm of the Kelvin wave at the equator and of 2.8 cm of the first-mode Rossby wave at 4°N.

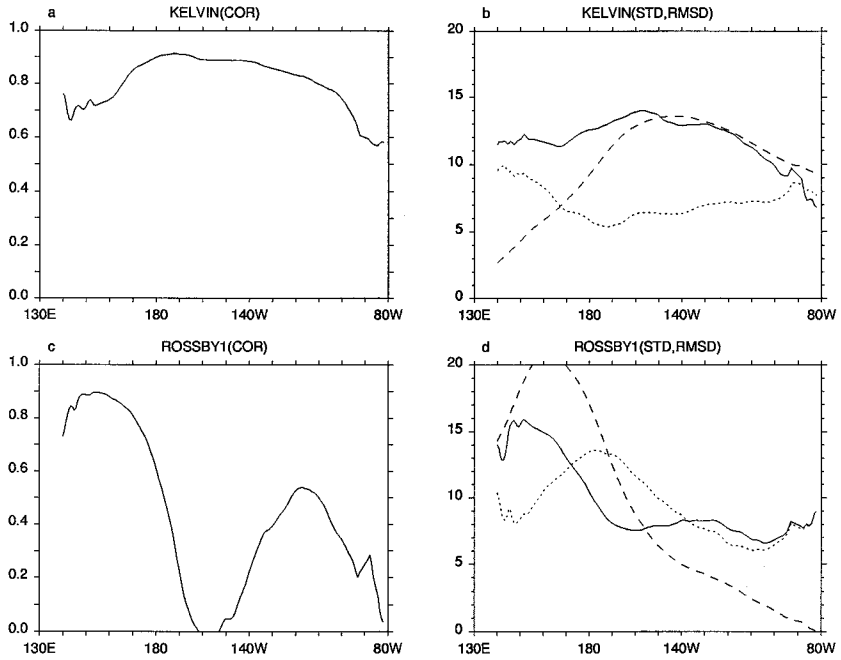

FIG. 7. (a) Correlation between OPA and SIMO Kelvin wave coefficients; (b) standard deviation of OPA (solid line) and SIMO (dashed line) Kelvin coefficients and rms difference (dotted line), noted RMSD, between both coefficients; (c) correlation between OPA and SIMO first-mode Rossby coefficients; and (d) standard deviation of OPA (solid line) and SIMO (dashed line) first-mode Rossby coefficients and rms difference (dotted line) noted RMSD between both coefficients.

ence between OPA and SIMO coefficients is higher from the date line to 160°W. We believe that the overestimation of the first-mode Rossby wave amplitude by our simple model is related to the vertical energy propagation described by Lukas and Firing (1985) and Kessler and McCreary (1993). Although their studies focused on the annual first-mode Rossby wave, we believe this mechanism to be at work in the model during the entire simulated period. While a detailed study of this mechanism in our OGCM will be needed, we can already provide some explanations. Kessler and McCreary (1993) simulated the first-mode Rossby wave as a sum of many of its vertical modes. As the higher vertical modes have slower vertical propagation, they are more likely to lose their energy. Considering the surface dynamic height anomalies to be actually a sum of many vertical modes, when projecting them onto the structure of the first baroclinic mode, leakage of energy from the high baroclinic modes is inevitable. Therefore, the first-mode Rossby wave amplitude simulated as the response of the first baroclinic mode only will not reproduce this loss of energy, and its signal will overestimate the first-mode Rossby wave amplitude calculated from OPA dynamic height anomalies with BM's method. In our simple wave model, the use of a strong damping coefficient (with a 3-month timescale) is then a crude way to simulate the loss of energy by vertical propagation as the Rossby wave propagates westward. We indeed observe the explained variance to increase when this damping timescale is increased to a value ranging between 1 and 3 months. We find here a strong limitation of describing even the sea surface variability with a single baroclinic mode model.

During the TOGA period, the ENSO events observed in the Pacific ocean are the El Niño events of 1986–87, 1991–92, and 1992–93 and the La Niña event of 1988–89. A warming period was also observed in late 1994. These interannual episodes are present in the OPA simulation, and the strongest equatorial waves forced during the ENSO events are fairly well simulated by our simple wave model. Indeed, comparison between Figs. 8a and 8b clearly shows that most of the Kelvin-type variability simulated in central and east Pacific is fairly well explained in terms of wind forcing. Both amplitude and phase are well reproduced by the simple wind-forced model. However, major differences are observed in the western Pacific where reflection may potentially play an important role. For the Rossby wave component (Figs. 9a and 9b), major differences are observed in the eastern Pacific, where signals reflected from incoming Kelvin waves may have a large contribution as well as near the western boundary, where the SIMO coefficient has too strong an amplitude.

First, preceding both the 1986–87 and 1991–92 El Niño events, the Kelvin wave signal in the western Pacific lacks strong downwelling amplitude (Fig. 8b).

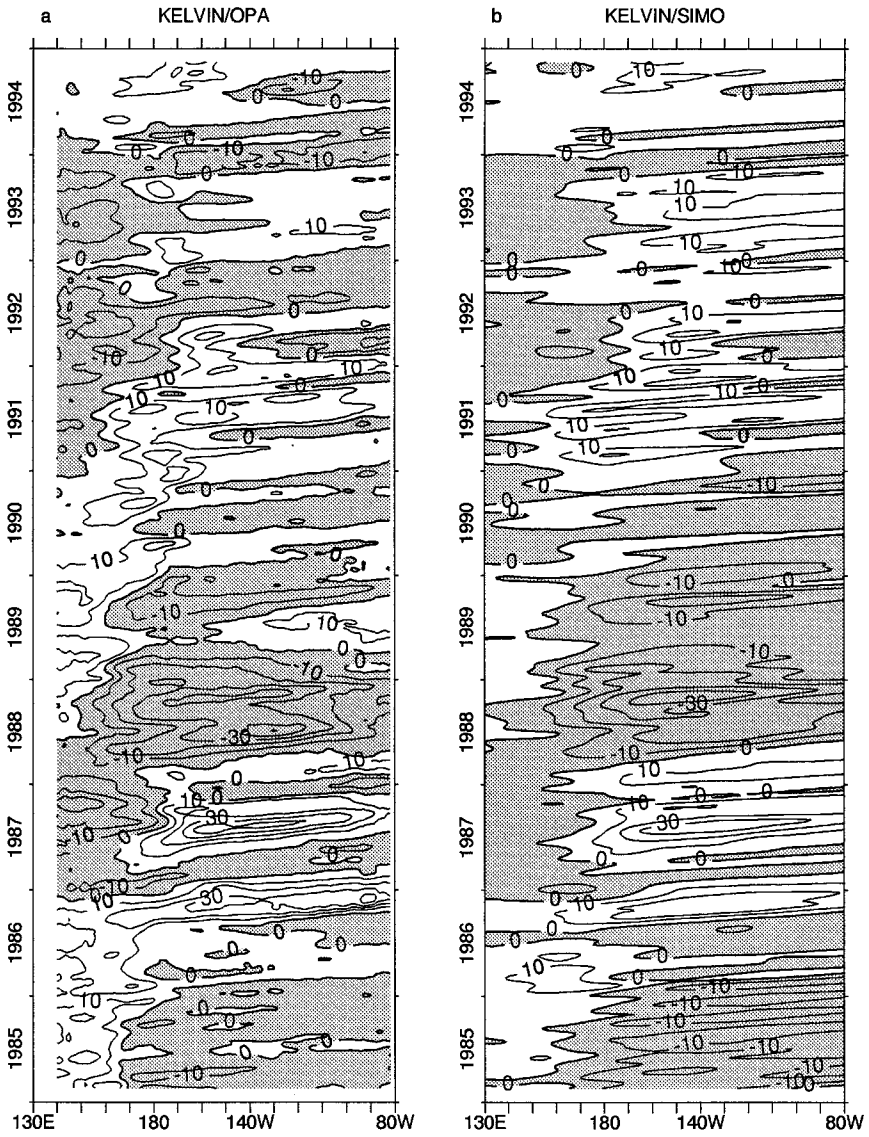

FIG. 8. Interannual anomalies of (a) OPA and (b) SIMO Kelvin wave coefficients. Coefficients are nondimensionalized. Contour intervals are every 10 units for the wave coefficients. An oceanic coefficient of 10 units would yield a dynamic height anomaly of 3.2 cm of the Kelvin wave at the equator.

From early 1985 to November 1986, the downwelling Kelvin signal is located from 130°E to the date line (Fig. 8a). This coherent signal over almost 2 years seems to be attributed to first-mode Rossby wave reflection at the western boundary. Indeed, strong downwelling first-mode Rossby waves are forced near the date line over this period (Figs. 9a and 9b). During the same period, upwelling Kelvin waves are generated to the east (Fig. 8b). This signal is not clearly seen in Fig. 8a, as downwelling Kelvin waves coming from western boundary reflection are superimposed to the negative amplitudes and nearly cancel them. A similar scenario is at work from the end of 1988 to the end of 1990. Strong downwelling first-mode Rossby waves are wind-forced near the date line and seem to reflect into downwelling Kelvin waves. Still considering Kelvin signals, other differences between Figs. 8a and 8b are seen at the end of 1987 and during the 1991–93 period. In July 1987, a strong westerly anomaly located near the date line generated a downwelling Kelvin wave and an upwelling first Rossby wave. The latter reached the western boundary at the end of 1987 simultaneously with the generation of an upwelling Kelvin signal in this region. During the 1991–93 period, upwelling first-mode Rossby waves are wind forced near the date line and seem to be responsible for the upwelling Kelvin signals ob-

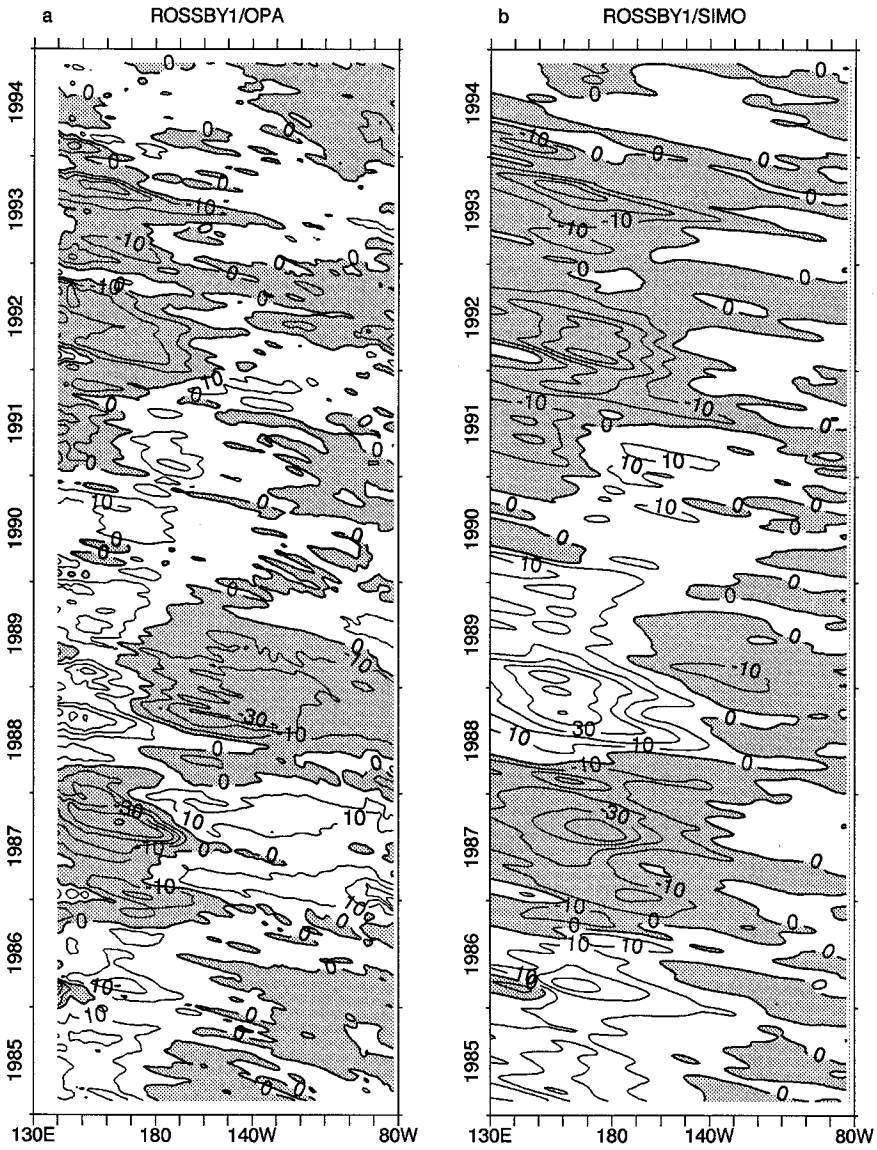

FIG. 9. As in Fig. 8 but for OPA and SIMO first-mode Rossby wave coefficients. Coefficients are nondimensionalized. Contour intervals are every 10 units for the wave coefficients. An oceanic coefficient of 10 units would yield a dynamic height anomaly of 2.8 cm of the first-mode Rossby wave at 4°N.

served in Fig. 8a and not present in Fig. 8b. These differences between OPA and SIMO Kelvin coefficients indicate that western boundary reflection exists and plays a role in the low-frequency variability of our oceanic general circulation model simulation.

In Figs. 9a and 9b, it can be seen that the downwelling Rossby signal observed in the western Pacific roughly from 1985 to fall 1986 prior to the 1986–87 El Niño event and from mid-1988 to late 1990 prior to the 1991–93 El Niño event is indeed wind forced. Major differences are observed during the 1986–89 period. In the beginning of 1987 and during the second half of that year, strong downwelling first-mode Rossby signals are observed coming from the eastern boundary. They are in phase with a potential reflection of strong downwelling Kelvin waves forced in late 1986 and in July 1987. Later during the 1988–89 La Niña event, the strong upwelling Rossby wave signal is not observed in Fig. 9b but is coherent with the arrival of strong upwelling Kelvin waves at the eastern boundary. Other differences between Figs. 9a and 9b seem to be attributable to Kelvin wave reflection at the eastern boundary. Eventually, the downwelling signal in 1988–89 in the western Pacific is much stronger in SIMO than in OPA coefficients. This difference may be due to the lack of upwelling Rossby waves coming from the Kelvin wave

reflection and subsequent propagation to the western Pacific. It is also surely related to the overestimation of the first-mode Rossby wave by the simple model as stated above.

6. Discussion and conclusions

Long equatorial waves have been shown to play an important role in variations of sea level (or dynamic height), zonal geostrophic current, and, possibly, sea surface temperature in the tropical Pacific Ocean. In this paper, we have examined an OGCM simulation of the tropical Pacific Ocean during the 1985–94 TOGA period with similar techniques as applied to observations. We first presented Kelvin and first-mode Rossby wave variability during the TOGA period, described the contribution of wind forcing to the wave signal, and gave some indications of potential reflections at both eastern and western boundaries. Moreover, differences between our simulation and the simple wave model allowed us to draw some limitations of interpreting sea surface variability with a single baroclinic mode model.

The simulation was performed with the OGCM developed at the LODYC (Delecluse et al. 1993) and adapted to the Pacific Ocean by Maes et al. (1997). Our present version covers the three tropical oceans between 50°N and 50°S. The forcing fields are taken from a simulation of the TOGA period by the climate version of ARPEGE. We focus on zonal wind stress and dynamic height (relative to 1000 db) fields filtered with a 55-day Hanning filter.

Both zonal wind stress and dynamic height fields are decomposed in terms of long equatorial waves using the methods described by Boulanger and Menkes (1995). Kelvin and first-mode Rossby wave propagations are observed at phase speeds typical of a first baroclinic vertical mode. Zonal wind stress and dynamic height fields are reconstructed considering only Kelvin and first-mode Rossby contributions and are then compared to the original fields. While only zonal wind stress variability in a narrow band around the equator (2°N–2°S) is well reproduced by the reconstructed field, dynamic height variance in a 5°N–5°S band is fairly well explained by the two equatorial waves. However, it is worth noting that strong off-equator signals cannot be represented. Besides, examination of the seasonal signal and interannual anomalies leads to the conclusion that Kelvin and first-mode Rossby wave seasonal signals are stronger east of the date line while interannual anomalies are more important west of the date line.

To describe interannual anomalies and potentially important reflections at both eastern and western boundaries, wave forcing coefficients are integrated along Kelvin and first-mode Rossby wave characteristics assuming a phase speed of 2.5 m s^{-1}. No reflection at both boundaries is taken into account in this simple wind-forced model (called SIMO). First, we found that the OPA Kelvin wave coefficient could be fairly well explained by the Kelvin wave simulated by the simple model. However, in terms of first-mode Rossby wave, the comparison is poor in the central Pacific between the two regions of strong zonal wind stress variability. It appears that the simple wave model is overestimating the wave amplitude along its propagation. This feature seems related to the vertical energy propagation described by Lukas and Firing (1985) and Kessler and McCreary (1993). This is thus a drawback in the interpretation of sea level–dynamic height variability in terms of long equatorial waves of a single baroclinic mode. Whether this feature is the result of our model physics, of the simulated ocean conditions due to the atmospheric forcing, or can be found in the real ocean will have to be investigated. Finally, the described discrepancies between OPA and SIMO wave coefficients over the TOGA period clearly show that SIMO wave coefficients cannot explain the Kelvin wave amplitude near the western boundary and the first-mode Rossby wave amplitude near the eastern boundary. Hence, in this model, Kelvin wave reflection at the eastern boundary and first-mode Rossby wave reflection at the western boundary play a role in the simulated central Pacific interannual variability. The reflection efficiency of both eastern and western boundaries in the model will have to be estimated and compared to observations.

Acknowledgments. The research described in this paper is the last part of Jean-Philippe Boulanger's thesis. He gratefully thanks ORSTOM (Institut Français de Recherche Scientifique pour le Développement en Coopération) for supporting him during these few years. Funding for this study was also provided by PNEDC (Programme National d'Etude dela Dynamique du Climat). The atmospheric forcing was provided by the CNRM (Centre National de Recherche de Meteo France). Support for computation was provided by the Conseil Scientifique of the IDRIS (Institut du Développement et des Ressources en Informatique Scientifique). The termination of this work was carried out while Jean-Philippe Boulanger was at the Jet Propulsion Laboratory/California Institute of Technology, under contract with the National Aeronautics and Space Administration. The authors are very appreciative of Lee-Lueng Fu for allowing Jean-Philippe Boulanger to finish this study. The technical discussions with Denise Kriesel are acknowledged. Finally, the authors wish to thank Roger Lukas and an anonymous reviewer for their fruitful comments that considerably helped us improve the original manuscript.

REFERENCES

Arakawa, A., 1972: Design of the UCLA general circulation model. Numerical simulation of weather and climate. Dept. of Meteorology, University of California, Rep. 7, 116 pp.

Asselin, R., 1972: Frequency filter for time integration. *Mon. Wea. Rev.*, **100,** 487–490.

Battisti D. S., 1988: Dynamics and thermodynamics of a warming

event in a coupled tropical atmosphere–ocean model. *J. Atmos. Sci.,* **45,** 2889–2919.

Blanke, B., and P. Delecluse, 1993: Variability of the tropical Atlantic Ocean simulated by a general circulation model with two different mixed-layer physics. *J. Phys. Oceanogr.,* **23,** 1363–1388.

Boulanger, J.-P., and C. Menkes, 1995: Propagation and reflection of long equatorial waves in the Pacific Ocean during the 1992–1993 El Niño. *J. Geophys. Res.,* **100,** 25 041–25 059.

Dandin, P., 1993: Variabilité basse fréquence simulée dans le Pacifique tropical. Thèse de Doctorat, l'Université Paris VI, 342 pp. [Available from LODYC, Université Paris VI, 75252 Paris, France.]

Delcroix, T., J. Picaut, and G. Eldin, 1991: Equatorial Kelvin and Rossby waves evidenced in the Pacific Ocean through GEOSAT sea level and surface current anomalies. *J. Geophys. Res.,* **96**(Suppl.), 3249–3262.

——, J.-P. Boulanger, F. Masia, and C. Menkes, 1994: GEOSAT-derived sea level and surface-current anomalies in the equatorial Pacific, during the 1986–1989 El Niño and La Niña. *J. Geophys. Res.,* **99,** 25 093–25 107.

Delecluse, P., G. Madec, M. Imbard, and C. Levy, 1993: OPA version 7 ocean general circulation model reference manual. Rapport Interne LODYC 93/05, 111 pp. [Available from LODYC, Université Paris VI, 75252 Paris, France.]

Déqué, M., C. Dreveton, A. Braun, and D. Cariolle, 1994: The ARPEGE/IFS atmosphere model: A contribution to the French community climate modeling. *Climate Dyn.,* **10,** 249–266.

Giese, B. S., and D. E. Harrison, 1990: Aspects of the Kelvin wave response to episodic wind forcing. *J. Geophys. Res.,* **95,** 7289–7312.

Jerlov, N. G., 1968: *Optical Oceanography*. Elsevier, 194 pp.

Kessler, W. S., and J. P. McCreary, 1993: The annual wind-driven Rossby wave in the subthermocline equatorial Pacific. *J. Phys. Oceanogr.,* **23,** 1192–1207.

——, and M. J. McPhaden, 1995: Oceanic equatorial waves and the 1991–1993 El Niño. *J. Climate,* **8,** 1757–1774.

Knox, R. A., and D. Halpern, 1982: Long range Kelvin wave propagation of transport variations in Pacific Ocean equatorial currents. *J. Mar. Res.,* **40**(Suppl.), 329–339.

Levitus, S., 1982: *Climatological Atlas of the World Ocean.* NOAA Prof. Paper 13, 173 pp.

Lukas, R., and E. Firing, 1985: The annual Rossby wave in the central equatorial Pacific Ocean. *J. Phys. Oceanogr.,* **15,** 55–67.

——, S. P. Hayes, and K. Wyrtki, 1984: Equatorial sea level response during the 1982–1983 El Niño. *J. Geophys. Res.,* **89,** 10 425–10 430.

Maes, C., G. Madec, and P. Delecluse, 1997: Sensitivity of an equatorial Pacific OGCM to the lateral diffusion. *Mon. Wea. Rev.,* **125,** 958–971.

Marti, O., G. Madec, and P. Delecluse, 1992: Comment on ''Net diffusivity in ocean general circulation models with nonuniform grids.'' *J. Geophys. Res.,* **97,** 12 763–12 766.

McPhaden, M. J., 1993: TOGA-TAO and the 1991–93 El Niño–Southern Oscillation event. *Oceanography,* **6,** 36–44.

Menkes, C., J.-P. Boulanger, and A. J. Busalacchi, 1995: Evaluation of TOPEX/POSEIDON sea level and basin-wide TOGA-TAO sea–surface topographies and derived geostrophic currents. *J. Geophys. Res.,* **100,** 25 087–25 099.

Miller L., R. Cheney, and B. Douglas, 1988: GEOSAT altimeter observations of Kelvin waves and the 1986–1987 El Niño. *Science,* **239,** 52–54.

Millero, F. S., and A. Poisson, 1981: An international one-atmosphere equation of state of sea water. *Deep-Sea Res.,* **28A,** 625–629.

Neelin, J. D., 1991: The slow sea surface temperature mode and the fast-wave limit: Analytic theory for tropical interannual oscillations and experiments in a hybrid coupled model. *J. Atmos. Sci.,* **48,** 584–606.

Oberhuber, J. M., 1988: An atlas based on the COADS data set: The budgets of heat, buoyancy and turbulent kinetic energy at the surface of the global ocean. Max-Planck-Institut für Meteorologie Rep. 15, 20 pp.

Paulson, C. A., and J. J. Simpson, 1977: Irradiance measurements in the upper ocean. *J. Phys. Oceanogr.,* **7,** 952–956.

Picaut, J., and T. Delcroix, 1995: Equatorial wave sequence associated with warm pool displacements during the 1986–1989 El Niño–La Niña. *J. Geophys. Res.,* **100,** 18 393–18 408.

——, C. Menkes, J.-P. Boulanger, and Y. du Penhoat, 1993: Dissipation in a Pacific equatorial long wave model. *TOGA-Notes,* **10,** 11–15. [Available from Nova University, Oceanographic Center, 8000 North Ocean Drive, Dania, FL 33004.]

Reynolds, R. W., and T. M. Smith, 1994: Improved global sea surface temperature analyses using optimum interpolation. *J. Climate,* **7,** 929–948.

Ripa, P., and S. Hayes, 1981: Evidence for equatorially trapped waves in the Galapagos Islands. *J. Geophys. Res.,* **86,** 6509–6516.

Schopf, P. S., and M. J. Suarez, 1988: Vacillations in a coupled ocean–atmosphere model. *J. Atmos. Sci.,* **45,** 549–566.

Stockdale, T., D. Anderson, M. Davey, P. Delecluse, A. Kattenberg, Y. Kitamura, M. Latif, and T. Yamagata, 1993: Intercomparison of tropical Pacific Ocean GCM'S. WCRP 79, WMO/TD-545, 43 pp. [Available from Joint Planning Staff for WCRP, c/o World Meteorological Organization, Case Postale No. 2300, CH-1211 Geneva 20, Switzerland.]

Wyrtki K, 1975: El Niño—The dynamic response of the equatorial Pacific ocean to atmospheric forcing. *J. Phys. Oceanogr.,* **5,** 572–584.